Journal of Materials Research and Technology 27 (2023) 2893–2901

Contents lists available at ScienceDirect

Journal of Materials Research and Technology

journal homepage: www.elsevier.com/locate/jmrt

Grain refinement of Ti6Al4V by incorporating in-situ TiB nanowhiskers in laser melting deposition

Ke Fu [a], Yuyu Liu [a,b], Yeqing Wang [a,***], Zhe Xu [a], Wei Jiang [a], Zheng Chen [a,**], Siqi Liu [b], Li Sun [c], Zhiliang Zhang [b], Jianying He [b,*]

[a] School of Materials Science and Physics, China University of Mining and Technology, Xuzhou, 221008, China
[b] Department of Structural Engineering, Norwegian University of Science and Technology (NTNU), Trondheim 7491, Norway
[c] School of Mechanical and Aerospace Engineering, Nanyang Technological University, 639798, Singapore

ARTICLE INFO

Keywords:
Titanium matrix composites
Laser melting deposition
Microstructure evolution
Grain refinement

ABSTRACT

One of the known problems in laser melting deposition (LMD) of alloys is columnar grain morphology and large grain size. Adding reinforcements is generally suggested as a viable approach to tailor the microstructure and enhance mechanical properties. However, quantitative relationships between grain morphology and reinforcement content are sparsely available. In this study, TiB_2 particles with different weight ratios were applied in the LMD of Ti6Al4V alloy to investigate its impact on grain refinement. It shows that the increasing TiB_2 content enhances the equiaxed grain growth from epitaxial growth and reduces the grain size. A linear function between decreasing grain size and the inverse of the growth restriction factor originating from TiB_2 content was obtained. This was attributed to the heterogenous nucleation of in-situ TiB nanowhiskers that promoted the refinement of α lath and prior β grain. The results shed new light on controlling grain morphology and predicting grain size by mixing ceramic-metal materials in LMD additive manufacturing.

1. Introduction

Additive manufacturing (AM) has been extensively utilized to fabricate titanium alloys with dual (α+β) phase because of its superiority in near net shape process [1–4]. Due to the high flexibility and customization of AM technology, it is feasible to fabricate titanium matrix composites (TMCs), hybrid, and functionally graded materials [5–7]. Among the various categories of AM processes, laser melting deposition (LMD) is a coaxial printing technology with energy-effective, finely controlled, and low-cost advantages. However, the solidification conditions of the molten pool during LMD are commonly associated with ultra-high cooling rates and thermal gradient, leading to the formation of columnar grain that is detrimental to mechanical properties [8,9]. Therefore, a key challenge in AM titanium-based alloys process is to promote the transformation from columnar to equiaxed grains.

The columnar grains are generally prior β-grains, precipitating from the liquid phase and growing epitaxially. It is caused by a lack of nucleation agents and extreme thermal conditions. Some reports attempt to increase heterogeneous nucleation by manipulating the processing parameters. Zhang et al. [10] reported that the microstructure of Ti–6Al–2Zr–2Sn–3Mo-1.5Cr–2Nb was dominated by columnar grains for a large range of parameters via laser additive manufacturing, and equiaxed grains were only observed under a high feed rate. Wang et al. [11] obtained Ti6Al4V with columnar and equiaxed grains by LMD under a high feed rate because it leads to more partially melted powders as endogenously heterogeneous nucleation sites. Besides, it is an efficient method to control microstructure by altering solidification conditions. Fan et al. [12] found the typical columnar grains of Ti6Al4V bulks by directed energy deposition with the synchronous induction heating method, even though the inductive energy apparently reduces the cooling rate and prolongs diffusion time. Those works indicate that the columnar to equiaxed transition (CET) for titanium alloys is difficult to realize by manipulating the printing parameters alone because potential particles and essential constitutional supercooling are not sufficient in the molten pools [13]. Several methods were proposed to advance the CET, such as adding nucleation agents and increasing

* Corresponding author.
** Corresponding author.
*** Corresponding author.
E-mail addresses: tbh281@cumt.edu.cn (Y. Wang), chenzheng1218@163.com (Z. Chen), jianying.he@ntnu.no (J. He).

https://doi.org/10.1016/j.jmrt.2023.10.128
Received 16 August 2023; Accepted 12 October 2023
Available online 15 October 2023

Table 1
Specified chemical compositions of Ti6Al4V and TiB_2.

Powder	Mass fraction (wt.%)							
Ti6Al4V	Ti	Al	V	Fe	C	H	O	N
	Bal.	6.12	4	0.3	0.08	0.012	0.18	0.04
TiB_2	TiB_2	H	O	C	S	Al	Fe	
	Bal.	0.02	0.04	0.01	0.02	0.02	0.01	

constitutional supercooling [14,15].

Ceramic materials can refine the prior β columnar grain of titanium-based alloys during the solidification where the size of β grain becomes one of the most significant structural factors [11,16]. Boride, especially TiB, is one of the promising reinforcements for titanium alloys to obtain TMCs with excellent performance. It ascribes that TiB and Ti share similar densities (4.51 and 4.54 g/cm^3), and thermal expansion coefficients (8.6×10^{-6} and 8.6×10^{-6} K^{-1}), ensuring thermal stability and compatibility of reinforcement with Ti matrix [17]. Attar et al. [15] fabricated Ti–TiB composites and obtained refined grains and enhanced tensile strength. Niu et al. [18] reported that TiB/(Ti–Fe) composite by LMD displayed a fully equiaxed grain morphology. Hu et al. [19] found TiB–Ti composites manufactured by LMD showing a three-dimensional quasi-continuous network (3DQCN) microstructure that was beneficial for strengthening and toughening of the composites. However, questions regarding the grain refinement mechanism and the optimal design of the TiB_2 addition remain unanswered.

In this work, the thermal history during LMD was characterized by finite element analysis under consistent processing parameters with experiment. TiB_2 powder was selected as the reinforcement in titanium matrix. The effect of in-situ TiB on the grain morphology and microstructure evolution was investigated to obtain the relationship between the quantity of addition and grain size. The orientation between in-situ TiB nanowhiskers and titanium matrix was also verified to explain the heterogenous nucleation mechanism.

2. Materials and methods

2.1. Powder material and preprocessing

The compositions of commercially purchased Ti6Al4V powder (Hangtian Haiying Inc., Harbin, CN) with a diameter of 50–150 μm and TiB_2 powder (Alading Inc., Shanghai, CN) with an individual particle size of 4–8 μm are presented in Table 1. According to the weight ratio, four samples were designed with different compositions of x wt.% TiB_2/Ti6Al4V ($x = 0$, 1, 3, and 5), which are denoted as TMC0, TMC1, TMC2, and TMC3. The raw materials were dried in a vacuum chamber at 80 °C for 6 h. Then, Ti6Al4V and TiB_2 powders were mechanically blended in a mixer for 6 h to make spherical Ti6Al4V coated by TiB_2 particles. Fig. 1a–b shows the as-received Ti6Al4V powders and TiB_2 particles. They were blended into the pre-treated powder for LMD, as shown in Fig. 1c. During the blending, Ti6Al4V powders keep the spherical shape for good fluidity.

2.2. Laser melting deposition

The LMD system (Fig. S1) consists of a laser generator, printing chamber, powder delivery, and shield gas, and computational control, as schematically shown in Fig. 2a. The oxygen content of the chamber is controlled below 200 ppm to avoid oxidization of TMCs during LMD. The as-mixed powder and shield gas were simultaneously ejected and deposited on the Ti6Al4V substrate. Fig. 2b shows the as-printed bulk

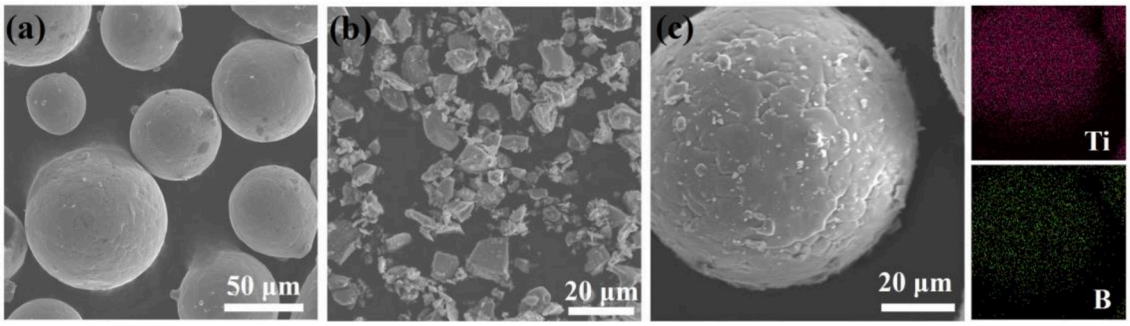

Fig. 1. SEM images of the raw powders (a, b) commercially purchased Ti6Al4V and TiB_2, (c) blended powder with TiB_2 particles coating Ti6Al4V and the elemental mapping.

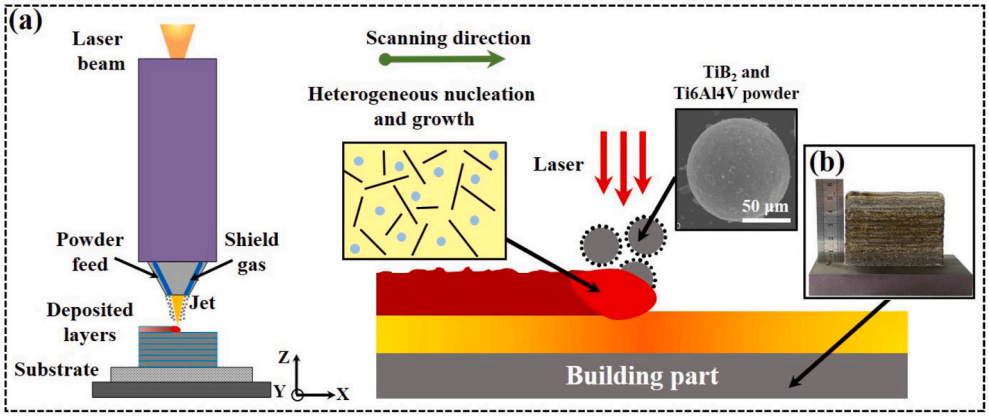

Fig. 2. Printing process and specimen geometry. (a) a schematic diagram for feeding blended powder and the deposition of TMCs by LMD process, (b) as-built thin wall bulk.

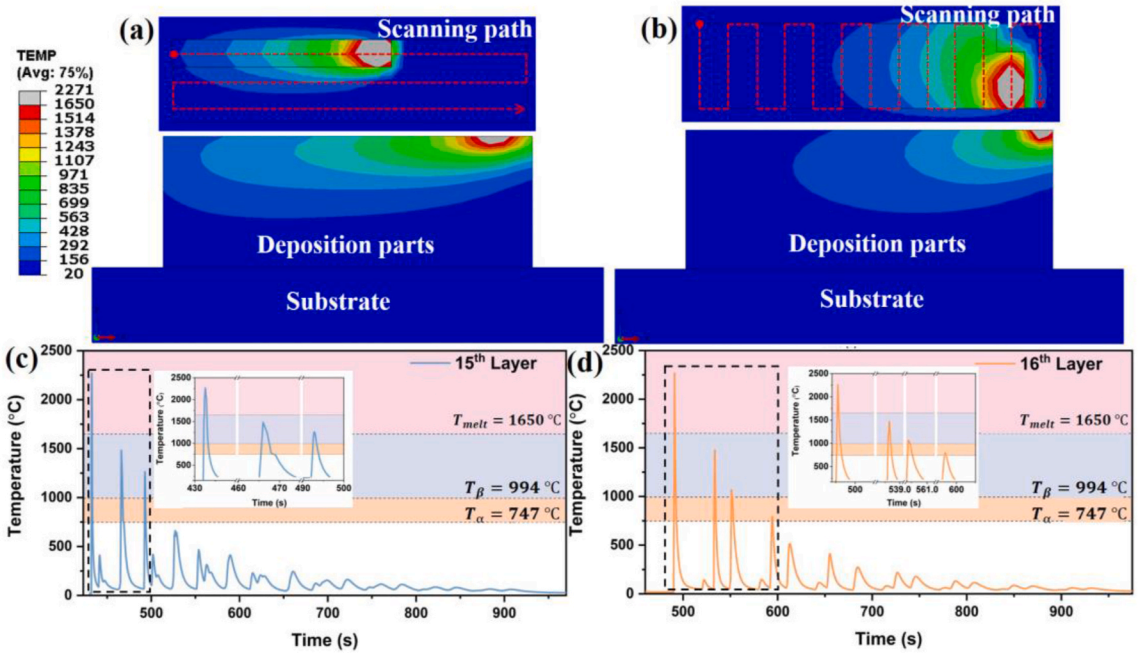

Fig. 3. Temperature distribution of TMC0 obtained from FEM (a, c) the 15th layer and (b, d) the16th layer (The red dotted arrow referring to the scanning path).

Table 2
LMD process parameters of Ti6Al4V and TMCs.

Laser power (W)	Scanning speed (mm/min)	Feeding rate (g/min)	Overlap rate (%)	Laser wavelength (μm)	Beam diameter (mm)
1800	360	6	50	1.07	3

with an approximate size of 70 × 12 × 55 mm. Two kinds of S-shaped scanning paths were used for fabrication, as shown in Fig. 3a–b. The printing paraments are listed in Table 2.

2.3. Microstructure characterization

For microstructure characterization, the cross-sectional samples were first polished by 0.05 μm colloidal silica, followed by etching with Kroll's reagent (10 % HF, 20 % HNO_3, 70 % H_2O) for 15 s. The microstructure of samples was observed by optical microscope (OM, Olympus-PMG3) and scanning electron microscope (SEM, Hitachi SU8220) equipped with energy dispersive spectrometry (EDS, Bruker, QUANTAX). The prior β grain size, TiB morphology, and α lath in the OM and SEM images were counted by software Image-Pro-Plus. The phase was identified by X-ray diffractometry (XRD, Bruker D8 Advance) with monochromatic Cu Kα radiation. Transmission electron microscope (TEM, JEM 2100) was used to characterize specific nanostructure and the selected area electron diffraction (SAED) patterns were captured at a 200 kV operating voltage. The crystallographic orientation was characterized via electron backscatter diffraction (EBSD).

2.4. Numerical simulation

The thermal analysis of the LMD process was simulated by the finite element method (FEM) with ABAQUS 2019. The simulation details were provided in the supplementary. Here, the adjacent 15th and 16th layers were chosen to show the temperature field and their intrinsic thermal cycles with a maximum temperature of 2271 °C, as shown in Fig. 3. The temperature field was divided into four regions, L region (T > 1650 °C, T_{melt}), β ⟺ α transition region (994 °$C \leq T \leq$ 1650 °C, T_β), α coarsening region (747 °$C \leq T \leq$ 994 °C, T_α) and unchanged region (T < 747 °C) [12,20].

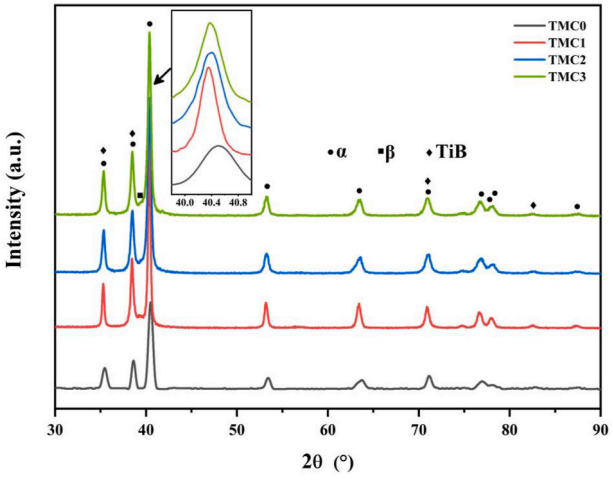

Fig. 4. XRD patterns for TMC0, TMC1, TMC2, and TMC3.

3. Results

3.1. Phase identification

The XRD patterns of the as-built TMCs samples are shown in Fig. 4. The phases α, β, and TiB are thus identified. The lattice parameter of the α phase is determined as $a = 2.94$ Å, $c = 4.67$ Å. The lattice parameters of the β phase and TiB are measured as 3.33 Å and 4.56 Å, respectively. It should note that the peaks for TiB_2 are not identified, indicating that TiB_2 has been reacted to form in-situ TiB. Besides, the inset shows that the main peaks at the angle of 40.5° of TMC1-TMC3 shift about 0.12° to the left than that of TMC0. This is attributed to the consumption of titanium by the in-situ reaction between Ti and TiB_2. The diffraction intensity at 40.5° of TMC0 is lower than that of the other TMCs. In addition, α′ martensite has formed in the matrix due to the non-equilibrium solidification conditions and is further verified by the

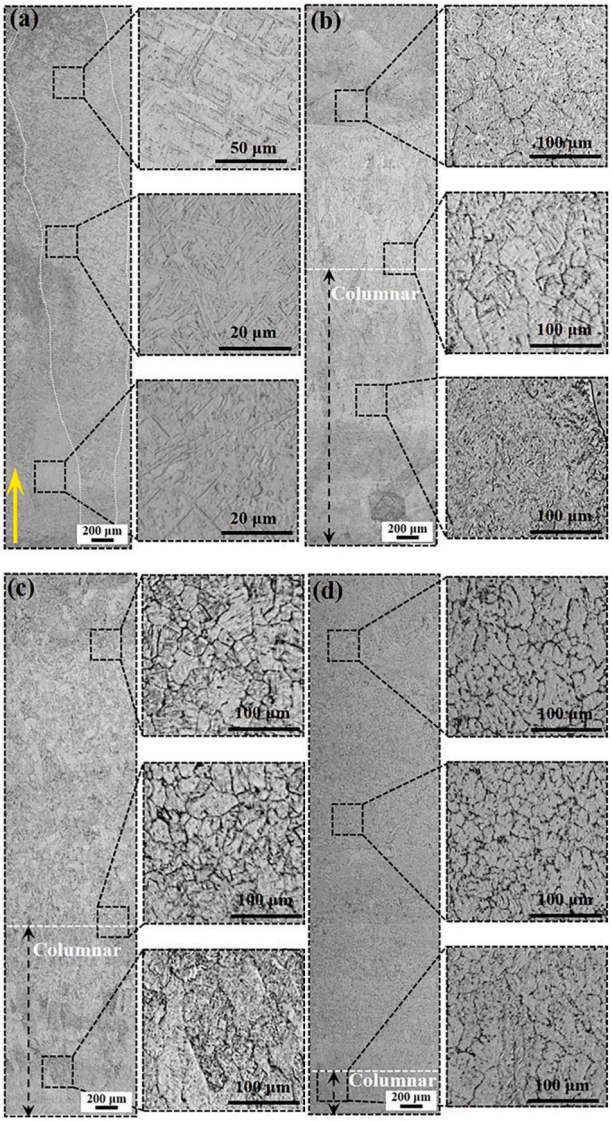

Fig. 5. OM microstructures of four samples with detailed inset of bottom, center, and top regions. (a) TMC0, (b) TMC1, (c) TMC2, (d) TMC3 (The yellow arrow refers to deposition direction and the same below.)

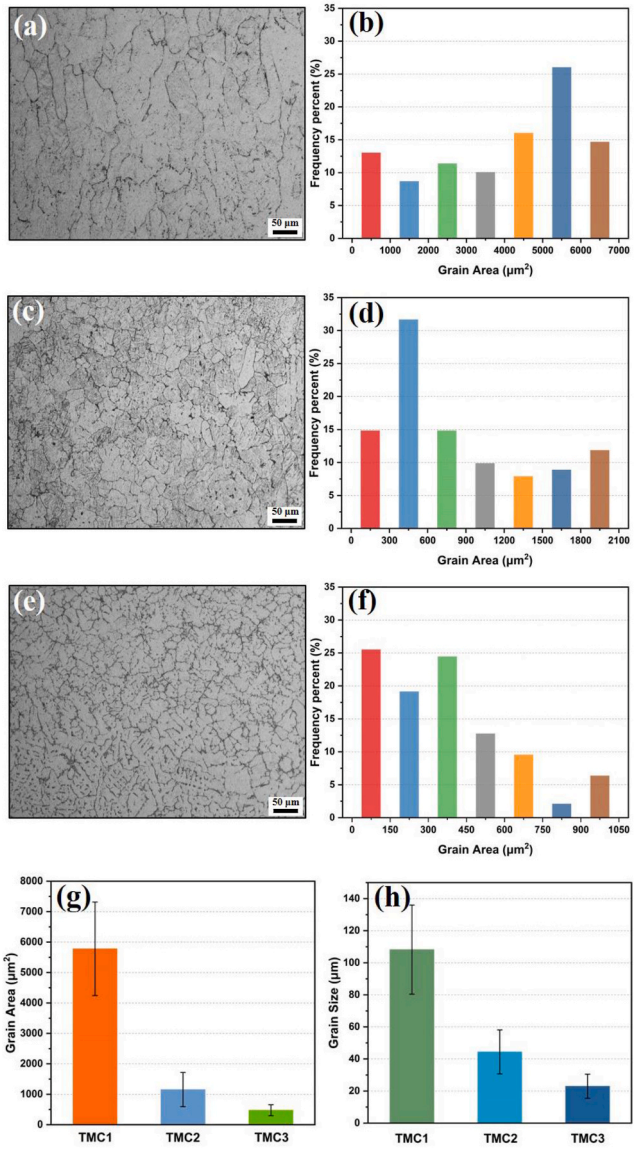

Fig. 6. OM and grain area distribution (a, b): TMC1 (c, d): TMC2 (e, f): TMC3 (g, h): Statistical results of grain area and size.

subsequent TEM results. However, the lattice parameters of the orthogonal α′ ($a = 2.9266$ Å, $c = 4.6677$ Å) are quite closed to that of the α phase.

3.2. Grain refinement and matrix evolution

Morphologies and microstructures of TMCs are characterized in detail by OM and SEM. In Fig. 5a, the white dotted line describes the typical coarse columnar β grains that grow epitaxially along the deposition direction (yellow arrow) of TMC0. The internal structure in the prior β grain shows a basket-weave morphology, as shown in the magnified images. Fig. 5b–d presents the microstructures of TMC1, TMC2, and TMC3. The penetrating columnar grains disappear at the center and top from TMC1-TMC3 samples. The magnified images depict that the grains are equiaxed, while the bottoms are columnar grains. The columnar grain region from the substrate is decreased from 2.5 to 1.7 and then to 0.4 mm. The center parts were chosen and counted to calculate grain area and grain size of equiaxed grains, as shown in Fig. 6a–f. Their average grain area reduces dramatically from 5780 ± 1535 to 1154 ± 563 and even 478 ± 181 μm^2, with average grain size decreasing from 105 ± 27 to 44 ± 13, 23 ± 8 μm, summarized in Fig. 6g–h.

Fig. 7 depicts the detailed SEM images of TMCs. The phase with dark contrast represents bamboo-like α lath while the region with bright contrast is the β phase. The microstructure within columnar prior β grains is delineated by α+β structure with lamellar basket-weave structure, agreeing with the previous work [21]. For TMC1-TMC3, the TiB whiskers distribute at the boundary of prior β grains showing self-joining shapes, hierarchical branches, and cross junctions, forming a three-dimensional quasi-continuous network (3DQCN) microstructure. Characteristic 3DQCN microstructure of TMC1 is shown in Figs. S1a-b. The chemical compositions and elemental mappings in Fig. S2 prove that the structure consists of the TiB-rich region. The microstructures of TMC2 and TMC3 are finer, as shown in Figs. S1c-d. They share similar elemental distribution pattern as TMC1. Fig. 7e shows the statistics of the α lath width from TMCs. Compared to the thickness of α laths from TMC0, the thickness of α laths from TMC1, TMC2, and TMC3 become thinner, which reduces from 1.4 ± 0.12 to 0.95 ± 0.15, 0.7 ± 0.14 μm, and 0.68 ± 0.1 μm. The aspect ratios of length to width for TiB in TMC1-TMC3 are 8.0 ± 2.3, 8.8 ± 3.3, and 7.6 ± 2.9, respectively, as

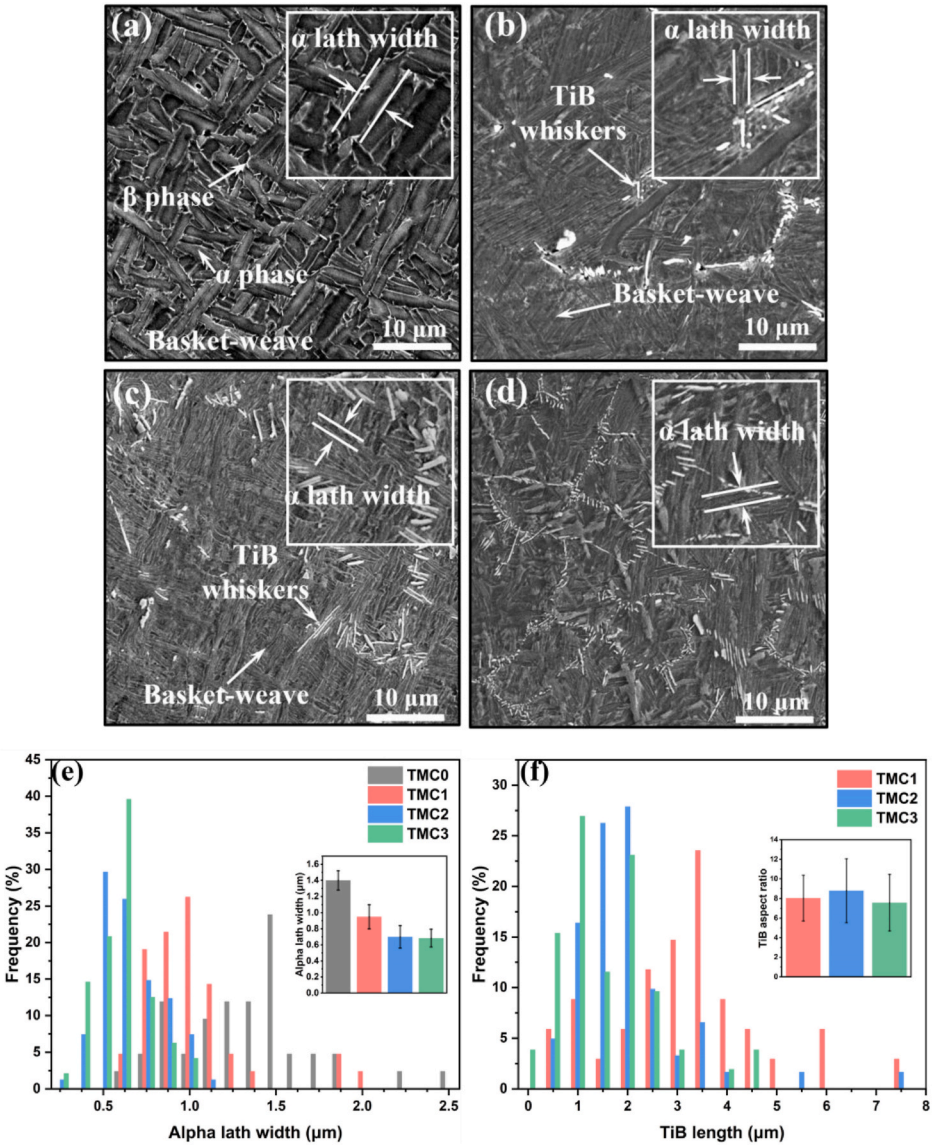

Fig. 7. SEM images of TMCs. (a) TMC0, (b) TMC1, (c) TMC2, (d) TMC3, (e) average α lath width and frequency percent of different TMCs, (f) frequency percent of TiB whisker length and aspect ratio for different TMCs.

shown in Fig. 7f.

3.3. Orientation between TiB and matrix

To understand the phase constituents and crystallographic orientation, the EBSD and TEM characterization were performed for the TMC3 sample. Fig. 8 displays the band contrast map, phase map, and inverse pole figure (IPF) maps. α, β, and TiB phases were identified. Fig. 8b shows the TiB whiskers are distributed at the grain boundary clearly, but the signal from the β phase is weak according to its unobvious diffraction peaks in Fig. 4. The structure tailored by in-situ TiB and refined α lath with an average size of 1.96 ± 0.9 μm is shown in Fig. 8c. The grain orientation indicates a weak texture due to the surpass of α variant selection during titanium phase transformation [22].

Fig. 9a–b manifest the bright-field TEM images of the titanium matrix that consists of basket-weave α+β and a few α′ martensites with slightly dark contrast. α phase shows no dislocation while there is a high density of tangled dislocations within α′ martensite [18]. Fig. 9e–g shows the SAED patterns from the Ti6Al4V matrix in the zone axes $[\bar{1}101]_{\alpha}$, $[011]_{\beta}$, and $[\bar{1}101]_{\alpha'}$, respectively. The transverse section of the in-situ TiB with the hexagonal shape shows (100), (101), and $(10\bar{1})$ planes, and longitudinal TiB grows along the [010] axis in Fig. 9c and d with $[010]_{TiB}$ zone axis in Fig. 9h.

Fig. 10a shows the interfacial boundary between transverse section TiB and β. high resolution TEM shows that the interplanar spacing of $(100)_{TiB}$ and $(110)_{\beta}$ are 0.46 nm and 0.232 nm, respectively. SAED patterns indicate the orientation relationship between TiB and β, is $(100)_{TiB}//(110)_{\beta}$, $[010]_{TiB}//[\bar{1}11]_{\beta}$. Fig. 10b–c shows the interfacial boundary of TiB/β and TiB/α. The in-situ TiB whisker embedded in the titanium matrix grows along $[010]_{TiB}$ and shows stacking faults. SAED patterns indicate the orientation relationship is $[010]_{TiB}//[001]_{\beta}$, $[010]_{TiB}//[11\bar{2}0]_{\alpha}$.

4. Discussion

4.1. Formation of the in-situ TiB reinforcements

The in-situ TiB whiskers are synthesized by the reaction during the heating process: $Ti + TiB_2 \rightarrow 2TiB$. The negative free energy and enthalpy of the reaction ensure that TiB_2 react with titanium matrix and generate

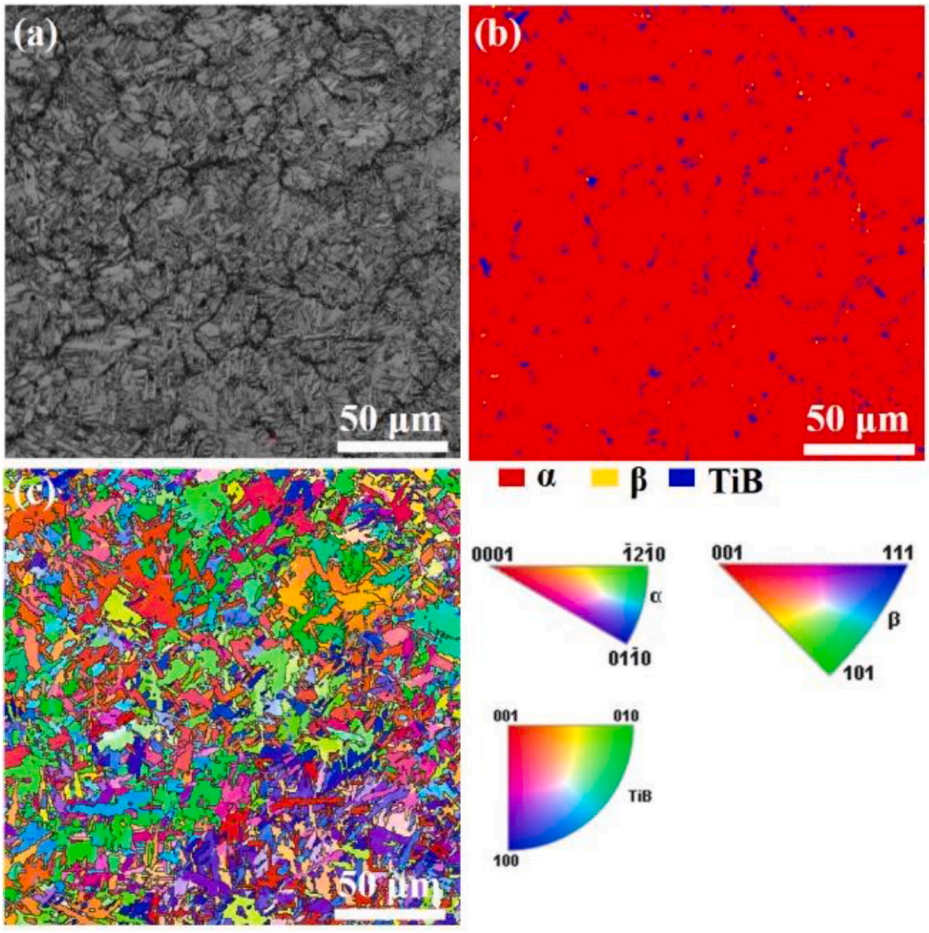

Fig. 8. EBSD results of TMC3. (a) band contrast (BC) map, (b) phase map, (c) inverse pole figure (IPF) map.

in-situ TiB with an exothermic process [23]. Besides, the raw TiB_2 particles show a size distribution of 4–8 μm (Fig. 1b), while in-situ reinforcements after the LMD process turn into whisker and needle shape (Figs. 7 and 10). The simulated maximum temperature during LMD is 2271 °*C*, which is above the melting temperature of TiB (2200 °*C*) [24]. Therefore, the blended powders (Fig. 1c) can melt and successfully trigger the in-situ reaction during LMD. The processing parameters for four samples were kept consistent during the LMD process and hence the temperature histories are nearly identical due to the similar physical parameter between TiB and Ti, such as density and coefficient of thermal expansion.

The length of TiB (along the [010]TiB direction) can be predicted by equations (1) and (2) [25]:

$$x = k\sqrt{t} \tag{1}$$

$$k = k_0 e^{\left(-\frac{Q_k}{2RT}\right)} \tag{2}$$

where x, k, and t are the TiB length, growth rate, and growth time, respectively; k_0, Q_k, R, and T are the constant (17.07×10^{-4} m $s^{-0.5}$), growth activation energy (190.3 kJ/mol), gas constant (8.314 J/(mol·K)), and temperature in Kelvin, respectively. The diffusion of the boron atom and TiB growth occur when temperature is above 830 °*C*. The length of TiB whiskers is proportional to growth time. It reported that the average length of TiB were 40–45 μm at 1300 °*C* and 10–15 μm at 1100 °*C* for 2 h [26]. In this work, the growth time for TiB is not sufficient during the LMD process. As shown in Fig. 3c and d, the time of the temperature above 830 °*C* lasted for approximate 4.6 s in the circulating heating curves, which leads to the nanosize scale TiB rods. The distinction of aspect ratio in TMC1-TMC3 is not obvious with 8.0 ± 2.3, 8.8 ± 3.2, and 7.6 ± 2.8, respectively.

4.2. Nucleation mechanism

The nonequilibrium sequence of solidification for TMCs during the LMD process is expected to be as follows:

$$Liquid\ (Ti+B) \rightarrow Liquid + TiB \rightarrow \beta(Ti) + TiB \rightarrow \alpha\,/\,\alpha'(Ti) + \beta(Ti) + TiB$$

As shown in Fig. 3, the temperature of β→α transformation starts at 994 °*C* under the non-equilibrium solidification process [27]. On the one side, in-situ TiB whiskers precipitate around prior β grain boundaries below T_{melt} and tailor the coarse columnar into the 3DQCN structure (Fig. 7). Therefore, the β phase well follows the Burgers orientation relationship with $(100)_{TiB}//(110)_{\beta}$, $[010]_{TiB}//[\bar{1}11]_{\beta}//[11\bar{2}0]_{\alpha}$ as shown in Fig. 10. On the other side, In-situ TiB can also be regarded as the potential heterogeneous nucleation particles of equiaxed grains. The lattice misfit (δ) between TiB and β is calculated by the following Turnbull–Vonnegut equations (3) and (4) [28]:

$$\delta = \frac{|d_m - d_p|}{d_p} \tag{3}$$

$$\delta^{(hkl)_s}_{(hkl)_n} = \sum_{i=1}^{3} \frac{\left|\left(d_{[uvw]^i_s}\cos\theta\right) - d_{[uvw]^i_s}\right| \Big/ d_{[uvw]^i_n}}{3} \times 100\% \tag{4}$$

where d_m and d_p are the interatomic/interplanar distance of nucleus plane and crystallization plane, respectively. $(hkl)_s$ is a low–index plane

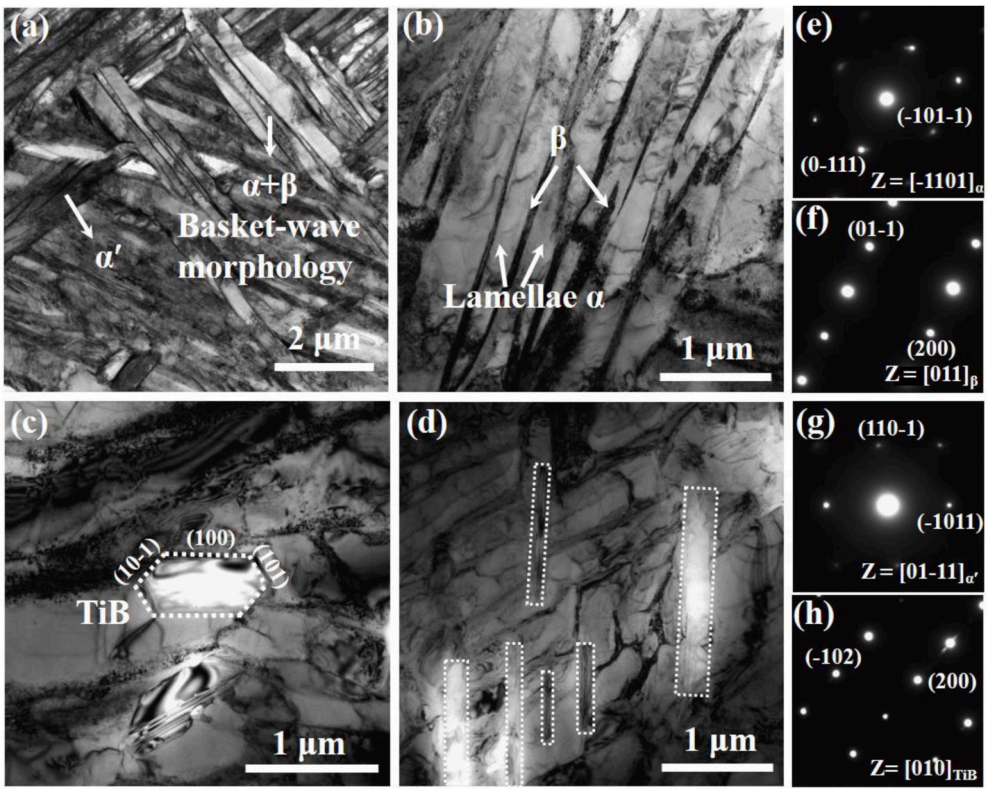

Fig. 9. The TEM images of TMC3 (a, b) bright-field images of the titanium matrix (c, d) bright-field images of the in-situ TiB with transverse and longitudinal sections (e–h) the corresponding SAED pattern of α, β, α′ and TiB.

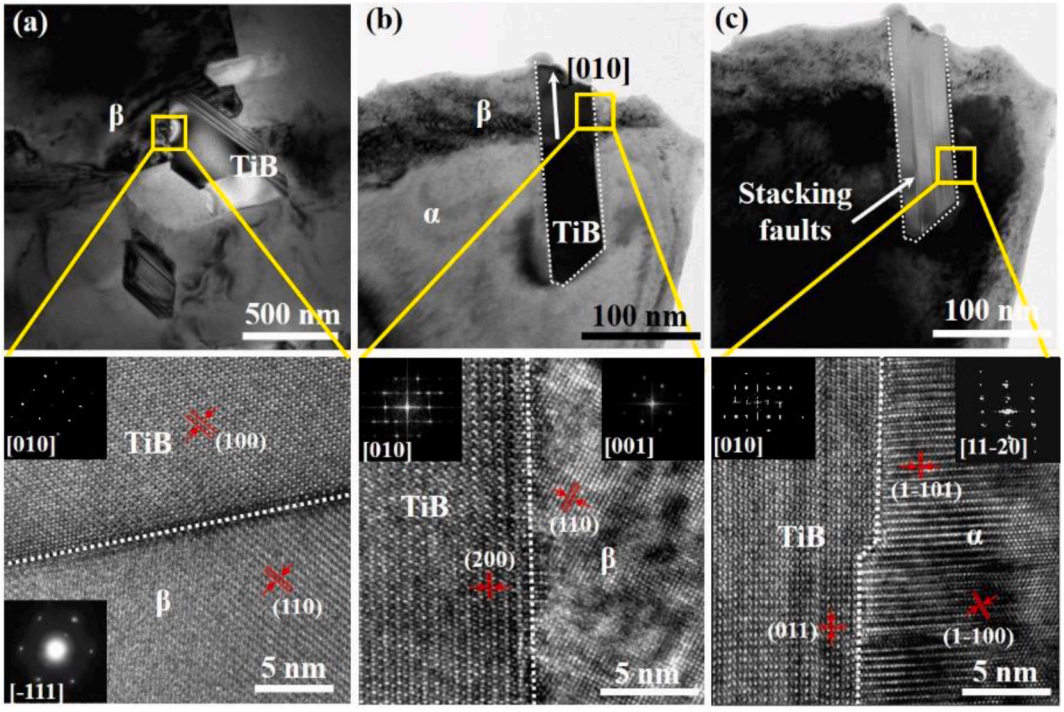

Fig. 10. TEM results of different interfaces for TMC3. (a) transverse section TiB and interfacial boundary between TiB/β-Ti (b, c) bright/dark field image of longitudinal section TiB with TiB/β-Ti and TiB/α-Ti interfacial boundary, respectively.

of the substrate, $(uvw)_s$ a low-index direction in $(hkl)_s$, $(hkl)_n$ a low–index plane of the nucleated solid, $[uvw]_n$ a low-index direction in $(hkl)_n$, $d_{[uvw]_s}$ the interatomic distance along $(uvw)_s$, $d_{[uvw]_n}$ the interatomic distance along $[uvw]_n$, and θ is the angle between the $(uvw)_s$ and $[uvw]_n$. The close-packed plane of TiB with B27 structure is $(100)_{TiB}$ with interplanar distance $d_{(100)} = 0.456$ nm and that of the prior β is $(110)_\beta$ with $d_{(110)} =$

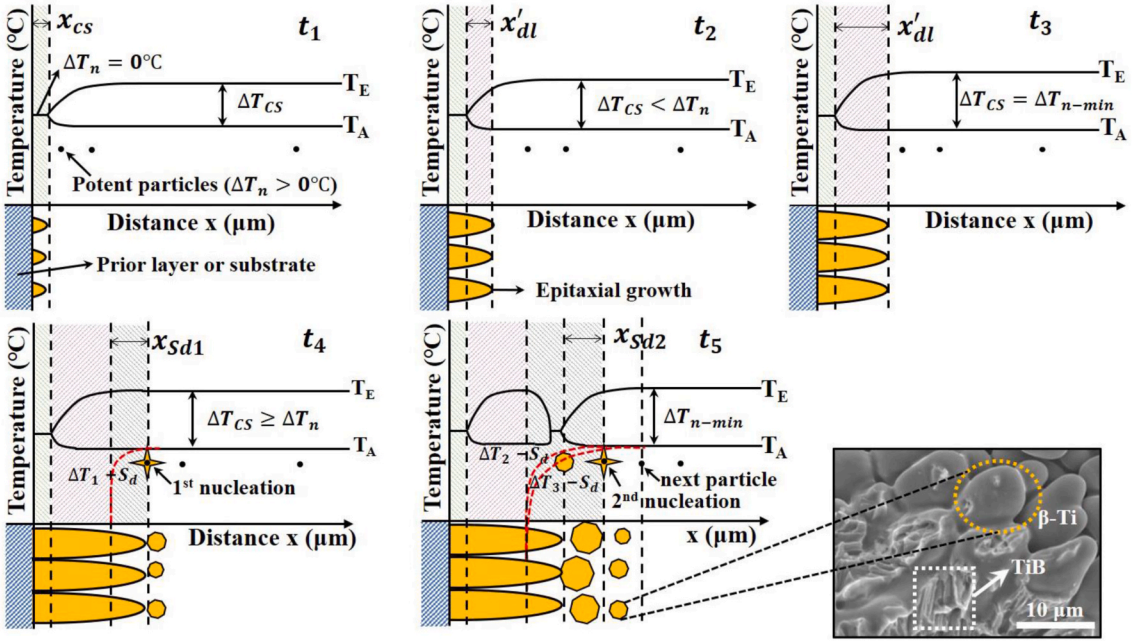

Fig. 11. A schematic diagram of the Independence Model illustrating the refinement of tailored grain at t_1-t_5 intervals for 3DQCN microstructure.

0.232 nm [29]. According to equation (3), the misfit of the orientation relationship is evaluated to be 1.72 % and 4.8 %, as shown in Fig. 10a and c. When the misfit is less than 6 %, the heterogeneous particles are the most effective and compatible nucleus [30]. Hence, the interfaces of TiB/β and TiB/α is the semi-coherent and the in-situ reaction can improve the interface bonding.

The heterogeneous nucleation can effectively reduce the interfacial energy and occurs at much lower undercooling in the perspective of classical nucleation theory [31]. The presence of large particles in the melt enables the liquid to wet a larger surface and form a thin hemispherical cap, effectively increasing its radius of curvature and facilitating further growth. Geer et al. [28] also found that TiB_2 particles with a diameter of 3 μm for aluminum alloy can provide high potency with maximum undercooling ($\Delta T_N \approx 0.2$ K), which is responsible for the most nucleation events. SEM images demonstrate (Fig. 7) that the morphology of the Ti–B compound changes from irregular shapes for TiB_2 to needle-like whiskers for TiB during the LMD process. Thus, the nucleation events and grain refinement can be attributed to the formation of in-situ TiB.

4.3. Grain refinement mechanism of 3DQCN microstructure

Some elements, such as B [32] and C [33], are growth restricting solutes for Ti solvent and play an important role in generating constitutional supercooling (ΔT_{CS}) that is determined by the growth restriction factor [34,35]. The Interdependence Model developed by StJohn et al. [36] is further used to reveal grain refinement mechanisms and predict grain size during AM process [13,37,38]. The grain refinement mechanism can be revealed by predicting grain diameter (d_{gs}) according to equation (6) [36]:

$$Q = mC_0(k-1) \tag{5}$$

$$d_{gs} = x_{CS} + x'_{dl} + x_{Sd} = \frac{Dz\Delta T_n}{vQ} + \frac{4.6D}{v}\left(\frac{C_l^* - C_0}{C_l^*(1-k)}\right) + x_{Sd} \tag{6}$$

where Q is the growth restriction factor, C_0 is the alloy composition (wt.%), m is the slope of the liquidus, k is the solute partition coefficient, D is the diffusion rate in the liquid, x is the distance and detailed in Fig. 11, v is the growth velocity, $z\Delta T_n$ is the incremental amount of undercooling required to re-establish ΔT_{n-min}, and C_l^* is the composition of the liquid at the S/L interface (wt.%). As illustrated in Fig. 11, the substrate or prior layer can provide the initial thermal undercooling ($\Delta T_n = 0\,^{\circ}C$) for epitaxial growth at t_1 when there is no constitutional supercooling (CS) or solute diffusion ahead of the S/L interface. x_{CS} refers to the distance that grain needs to grow to create sufficient CS to nucleate a grain. As the grains grow epitaxially and solute diffuses into liquid in the front of columnar grain, the temperature gradient decreases gradually and the amount of CS (ΔT_{cs}) increases from $\Delta T_{cs} < \Delta T_n$ at t_2 until a necessary threshold of $\Delta T_{cs} = \Delta T_{n-min}$ reached at t_3. x'_{dl} refers to the diffusion distance from the S/L interface to the position that establishes $\Delta T_{cs} = \Delta T_{n-min}$ which can activate potent particles with random distribution in the liquid. The microstructure changes from columnar to equiaxed grains until the potent particles are sufficient nearby. As shown in Fig. 5a, it is obvious that the grains of TMC0 without suitable nucleation particles show the epitaxial growth. Once the TiB_2 addition continues to increase, indicating high nucleation potency, the columnar length shortens dramatically, and the grains become refined (Fig. 5b–d).

At t_4 ($\Delta T_{cs} \geq \Delta T_{n-min}$), it shows the relationship of the average distance to the activated particles (x_{Sd}) with the undercooling (ΔT_n). Once the nucleation occurs and the grain grows, the subsequent equiaxed nucleation events are triggered (t_5). The SEM inset of TMC3 (Fig. 11) shows uniform equiaxed grains. It sufficiently proves that in-situ TiB whiskers adhered to the prior β can be considered as heterogeneous nucleation particles. Q is a useful parameter in predicting the relative grain refining effectiveness of various solutes in titanium alloy [39,40]. The theoretical calculation of $Q \approx 66\ C_0$ for boron in titanium is a reasonable approximation to the true value [32]. High Q value provides the grain-refining efficiency to establish CS zone and sharply decrease x_{CS} and x'_{dl}. The grain size (Fig. 6) shows a linear relationship against $1/Q$ for TMCs. The constitutional supercooling is caused by the rejection of boron from the prior β into the liquid ahead. Meanwhile, the potency particles and TiB whiskers are responsible for the enhanced nucleation and grain refinement.

5. Conclusion

Ti–6Al–4V component with 0, 1, 3, 5 wt.% additions of TiB_2 (TMC0,

TMC1, TMC2, and TMC3) were investigated and the findings are summarized as the following:

(1) The equiaxed growth prevailed instead of the epitaxial columnar with increasing TiB_2 content. A fully equiaxed grain morphology with the average grain size of 23 μm was obtained with the addition of TiB_2 up to 5 wt.%.
(2) In-situ TiB was generated by reacting with titanium matrix with nano-size due to the insufficient growth time. The nanowhiskers distributed at prior β grain boundaries to tailor a three-dimensional quasi-continuous network microstructure.
(3) In-situ TiB serves as compatible nucleation particles with small lattice misfits for both α and β phases resulting in the grain and titanium matrix refinement.
(4) The quantitative relationship between grain size and the inverse of growth restriction factor was established by the Interdependence model to predict grain size.

Declaration of Competing Interest

The authors declare that they have no known competing financial interests or personal relationships that could have appeared to influence the work reported in this paper.

Acknowledgement

The authors are grateful for funding from the Natural Science Foundation of China (51771226).

Appendix A. Supplementary data

Supplementary data to this article can be found online at https://doi.org/10.1016/j.jmrt.2023.10.128.

References

[1] Sridharan N, Wolcott P, Dapino M, Babu SS. Microstructure and texture evolution in aluminum and commercially pure titanium dissimilar welds fabricated using ultrasonic additive manufacturing. Scripta Mater 2016;117:1–5.
[2] Park H-K, Na T-W, Park JM, Kim Y, Kim G-H, Lee B-S, et al. Effect of cyclic heat treatment on commercially pure titanium part fabricated by electron beam additive manufacturing. J Alloys Compd 2019;796:300–6.
[3] Cui D, Zhang Y, He F, Ma J, Zhang K, Yang Z, et al. Heterogeneous microstructure of the bonding zone and its dependence on preheating in hybrid manufactured Ti-6Al-4V. Mater Res Lett 2021;9(10):422–8.
[4] Choi G, Choi WS, Han J, Choi P-P. Additive manufacturing of titanium-base alloys with equiaxed microstructures using powder blends. Addit Manuf 2020:36 101467.
[5] Zhang T, Huang Z, Yang T, Kong H, Luan J, Wang A, et al. In situ design of advanced titanium alloy with concentration modulations by additive manufacturing. Science 2021;374(6566):478–82.
[6] Tofail SAM, Koumoulos EP, Bandyopadhyay A, Bose S, O'Donoghue L, Charitidis C. Additive manufacturing: scientific and technological challenges, market uptake and opportunities. Mater Today 2018;21(1):22–37.
[7] Sun Z, Ji X, Zhang W, Chang L, Xie G, Chang H, et al. Microstructure evolution and high temperature resistance of Ti6Al4V/Inconel625 gradient coating fabricated by laser melting deposition. Mater Des 2020;191:108644.
[8] Zhang D, Sun S, Qiu D, Gibson MA, Dargusch MS, Brandt M, et al. Metal alloys for fusion-based additive manufacturing. Adv Eng Mater 2018;20(5):1700952.
[9] Carroll BE, Palmer TA, Beese AM. Anisotropic tensile behavior of Ti–6Al–4V components fabricated with directed energy deposition additive manufacturing. Acta Mater 2015;87:309–20.
[10] Zhang Q, Chen J, Wang L, Tan H, Lin X, Huang W. Solidification microstructure of laser additive manufactured Ti-6Al-2Zr-2Sn-3Mo-1.5Cr-2Nb titanium alloy. J Mater Sci Technol 2016;32(4):381–6.
[11] Wang T, Zhu YY, Zhang SQ, Tang HB, Wang HM. Grain morphology evolution behavior of titanium alloy components during laser melting deposition additive manufacturing. J Alloys Compd 2015;632:505–13.
[12] Fan W, Tan H, Zhang F, Feng Z, Wang Y, Zhang L-C, et al. Overcoming the limitation of in-situ microstructural control in laser additive manufactured Ti–6Al–4V alloy to enhanced mechanical performance by integration of synchronous induction heating. J Mater Sci Technol 2021;94:32–46.
[13] Bermingham MJ, StJohn DH, Krynen J, Tedman-Jones S, Dargusch MS. Promoting the columnar to equiaxed transition and grain refinement of titanium alloys during additive manufacturing. Acta Mater 2019;168:261–74.
[14] Hu Y, Zhao B, Ning F, Wang H, Cong W. In-situ ultrafine three-dimensional quasi-continuous network microstructural TiB reinforced titanium matrix composites fabrication using laser engineered net shaping. Mater Lett 2017;195:116–9.
[15] Attar H, Bönisch M, Calin M, Zhang L-C, Scudino S, Eckert JJAM. Selective laser melting of in situ titanium–titanium boride composites: processing, microstructure and mechanical properties. Acta Mater 2014;76:13–22.
[16] Liu Y, Xu H, Zhu L, Wang X, Han Q, Li S, et al. Investigation into the microstructure and dynamic compressive properties of selective laser melted Ti–6Al–4V alloy with different heating treatments. Mater Sci Eng, A 2021;805:140561.
[17] Attar H, Ehtemam-Haghighi S, Kent D, Dargusch MS. Recent developments and opportunities in additive manufacturing of titanium-based matrix composites: a review. Int J Mach Tool Manufact 2018;133:85–102.
[18] Niu J, Dai G, Guo Y, Sun Z, Dan Z, Dong Y, et al. Microstructure and mechanical properties of B modified Ti–Fe alloy manufactured by casting, forging and laser melting deposition. Compos Part B 2021;216:108854.
[19] Hu Y, Cong W, Wang X, Li Y, Ning F, Wang H. Laser deposition-additive manufacturing of TiB-Ti composites with novel three-dimensional quasi-continuous network microstructure: effects on strengthening and toughening. Compos Part B-Eng 2018;133:91–100.
[20] Ahmed T, Rack HJ. Phase transformations during cooling in α+β titanium alloys. Mater Sci Eng A 1998;243(1–2):206–11.
[21] Tan X, Kok Y, Tan YJ, Descoins M, Mangelinck D, Tor SB, et al. Graded microstructure and mechanical properties of additive manufactured Ti–6Al–4V via electron beam melting. Acta Mater 2015;97:1–16.
[22] Dai J, Xia J, Chai L, Murty KL, Guo N, Daymond MR. Correlation of microstructural, textural characteristics and hardness of Ti–6Al–4V sheet β-cooled at different rates. J Mater Sci 2020;55(19):8346–62.
[23] Zhang XN, Lu WJ, Zhang D, Wu RJ, Bian YJ, Fang PW. In situ technique for synthesizing (TiB + TiC)/Ti composites. Scripta Mater 1999;41(1):39–46.
[24] Hayat MD, Singh H, He Z, Cao P. Titanium metal matrix composites: an overview. Compos Part A-Appl S 2019;121:418–38.
[25] Fan Z, Guo ZX, Cantor B. The kinetics and mechanism of interfacial reaction in sigma fibre-reinforced Ti MMCs. Compos Part A-Appl S 1997;28(2):131–40.
[26] Panda K, Ravi Chandran KJM, A mt. Synthesis of ductile titanium-titanium boride (Ti-TiB) composites with a beta-titanium matrix: the nature of TiB formation and composite properties. Metall Mater Trans A 2003;34(6):1371–85.
[27] Cai C, Radoslaw C, Zhang J, Yan Q, Wen S, Song B, et al. In-situ preparation and formation of TiB/Ti-6Al-4V nanocomposite via laser additive manufacturing: microstructure evolution and tribological behavior. Powder Technol 2019;342:73–84.
[28] Greer AL, Cooper PS, Meredith MW, Schneider W, Schumacher P, Spittle JA, et al. Grain refinement of aluminium alloys by inoculation. Adv Eng Mater 2003;5(12):81–91.
[29] Feng H, Zhou Y, Jia D, Meng Q, Rao JJCg. design. Growth mechanism of in situ TiB whiskers in spark plasma sintered TiB/Ti metal matrix composites. Cryst Growth Des 2006;6(7):1626–30.
[30] Bramfitt BL. The effect of carbide and nitride additions on the heterogeneous nucleation behavior of liquid iron. Metall Trans A 1970;1(7):1987–95.
[31] Spittle JA. Columnar to equiaxed grain transition in as solidified alloys. Int Mater Rev 2006;51(4):247–69.
[32] Bermingham MJ, McDonald SD, StJohn DH, Dargusch MS. Beryllium as a grain refiner in titanium alloys. J Alloys Compd 2009;481(1–2):L20–3.
[33] Mereddy S, Bermingham M, Kent D, Dehghan-Manshadi A, StJohn D, Dargusch MJJ. Trace carbon addition to refine microstructure and enhance properties of additive-manufactured Ti-6Al-4V. JOM 2018;70(9):1670–6.
[34] Easton MA, StJohn DH. A model of grain refinement incorporating alloy constitution and potency of heterogeneous nucleant particles. Acta Mater 2001;49(10):1867–78.
[35] Mereddy S, Bermingham MJ, StJohn DH, Dargusch MS. Grain refinement of wire arc additively manufactured titanium by the addition of silicon. J Alloys Compd 2017;695:2097–103.
[36] StJohn DH, Qian M, Easton MA, Cao P. The Interdependence Theory: the relationship between grain formation and nucleant selection. Acta Mater 2011;59(12):4907–21.
[37] Chen Y, Yang C, Fan C, Zhuo Y, Lin S, Chen C. Grain refinement of additive manufactured Ti-6.5 Al-3.5 Mo-1.5 Zr-0.3 Si titanium alloy by the addition of La2O3. Mater Lett 2020;275:128170.
[38] Zhang D, Qiu D, Gibson MA, Zheng Y, Fraser HL, StJohn DH, et al. Additive manufacturing of ultrafine-grained high-strength titanium alloys. Nature 2019;576(7785):91–5.
[39] Easton M, StJohn D. An analysis of the relationship between grain size, solute content, and the potency and number density of nucleant particles. Metall Mater Trans A 2005;36a(7):1911–20.
[40] Greer AL, Bunn AM, Tronche A, Evans PV, Bristow DJ. Modelling of inoculation of metallic melts: application to grain refinement of aluminium by Al–Ti–B. Acta Mater 2000;48(11):2823–35.